BIOCHEMISTRY
including biophysical chemistry & molecular biology
Article

Biochemistry **2011,** *50,* 533–545 533
DOI: 10.1021/bi101558v

Enzymatic Adenylation of 2,3-Dihydroxybenzoate Is Enhanced by a Protein−Protein Interaction between *Escherichia coli* 2,3-Dihydro-2,3-dihydroxybenzoate Dehydrogenase (EntA) and 2,3-Dihydroxybenzoate-AMP Ligase (EntE)[†]

Sofia Khalil and Peter D. Pawelek*

Department of Chemistry and Biochemistry, Concordia University, 7141 Sherbrooke Street West, Montreal, Quebec, Canada H4B 1R6

Received September 24, 2010; Revised Manuscript Received December 8, 2010

ABSTRACT: The *Escherichia coli* siderophore enterobactin is synthesized in response to iron starvation. 2,3-Dihydro-2,3-dihydroxybenzoate dehydrogenase (EntA) produces 2,3-dihydroxybenzoate (DHB), a biosynthetic intermediate. 2,3-Dihydroxybenzoate-AMP ligase (EntE) adenylates DHB, activating it for attachment to the NRPS substrate holo-EntB. Using analytical ultracentrifugation, we found that EntA undergoes concentration-dependent dimer−tetramer self-association (K_D = 12.3 μM). We further found that EntA can form a specific complex with EntE. Pull-down assays revealed that recombinant EntA bait pulled down EntE from *E. coli* lysates, whereas recombinant EntE bait could pull down EntA. Addition of the SMCC cross-linker to a mixture of EntA and EntE resulted in a cross-linked product with a molecular mass of >250 kDa, suggesting a complex stoichiometry of one EntA tetramer and four EntE monomers. The effect of EntA on EntE activity was also examined. Addition of a 4-fold excess of EntA to an EntE assay mixture resulted in a 6-fold stimulation of EntE activity. EntA was also found to perturb the FRET signal between EntE donor residues and EntE-bound DHB. By following the EntA-dependent decrease in the magnitude of the EntE−DHB FRET signal, EntA−EntE binding behavior was found to be sigmoidal, suggesting the presence of both low- and high-affinity binding sites. The EntA−EntE interaction was also directly measured by isothermal titration calorimetry at 10 °C. The resulting binding isotherm fit well to a model describing two binding sites, supporting our AUC and fluorescence data. Taken together, our data show that tetrameric EntA optimally interacts with EntE, resulting in an enhancement of EntE activity.

Under iron-limiting conditions, most bacteria synthesize and secrete small molecules known as siderophores to obtain iron from the extracellular environment (*1*, *2*). Siderophores and the proteins involved in their synthesis, secretion, and modification are considered virulence factors in many pathogenic bacteria (*3*−*7*). In extraintestinal environments, *Escherichia coli* obtains ferric iron predominantly via the biosynthesis and secretion of enterobactin, a catecholate-type siderophore (*8*, *9*). Enterobactin consists of three 2,3-dihydroxybenzoic acid (DHB) moieties linked by amide bonds to three L-serine subunits cyclized in a triserine trilactone core (Scheme 1A). High-affinity chelation occurs through the hexadentate coordination of the three DHB catechol groups of enterobactin to one Fe^{3+} atom (association constant of $\sim 1 \times 10^{50}$ M^{-1}) (*10*). This extraordinary affinity for ferric iron is needed to effectively scavenge low-abundance extracellular Fe^{3+} and to compete with high-affinity chelators such as mammalian serum transferrin (*11*).

The biosynthesis and secretion of enterobactin require the proteins expressed from eight genes (*entA*−*F*, *entH*, and *entS*). Proteins encoded by the genes *fepA*−*G* then facilitate TonB-dependent uptake of ferric enterobactin from the extracellular environment. These genes are all under the control of the Fur repressor, such that expression is upregulated only when levels of intracellular iron are low (*12*−*14*). Enterobactin biosynthesis involves six enzyme activities that can be broadly grouped into two major segments that are functionally distinct (for a review, see ref *9*). The DHB synthesis segment includes the activities of EntC (*15*), EntB (the N-terminal isochorismatase domain) (*16*),

Scheme 1: (A) Chemical Structure of Enterobactin, (B) Reaction Catalyzed by *E. coli* 2,3-Dihydro-2,3-dihydroxybenzoate Dehydrogenase, and (C) Reaction Catalyzed by *E. coli* 2,3-Dihydroxybenzoate-AMP Ligase

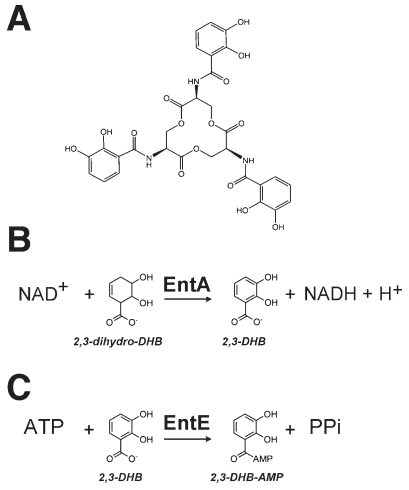

[†]This work was supported by Discovery Grant 341983-07 from the Natural Sciences and Engineering Research Council of Canada to P.D.P.

*To whom correspondence should be addressed. Telephone: (514) 848-2424, ext. 3118. Fax: (514) 848-2868. E-mail: ppawelek@alcor.concordia.ca.

© 2010 American Chemical Society

and 2,3-dihydro-2,3-dihydroxybenzoate dehydrogenase (EntA) (*17*); these activities function sequentially to catalyze the conversion of chorismate into DHB. The NRPS segment includes the activities of EntD (*18*), EntE (*19*), EntB [C-terminal aryl carrier protein (ArCP) domain], and EntF (*20*); activities in the NRPS segment function in concert to condense the three molecules each of DHB and L-serine into one enterobactin molecule (*21*, *22*). EntH has been shown to be a proofreading activity that ensures proper acylation of holo-EntB during the NRPS process (*23*, *24*). The inner-membrane protein EntS secretes enterobactin from the cytoplasm into the periplasm and is necessary for efficient enterobactin export (*25*).

We now know that the majority of proteins in a cell form specific complexes with one or more partner proteins to conduct their biological activities, and many such interactions are now targets in the development of novel chemotherapeutics (*26*−*29*). To what extent do protein−protein interactions play a role in enterobactin biosynthesis? Protein interactions within the NRPS segment have already been reported (*22*, *30*−*33*). The rate of DHB adenylation by EntE was shown to increase in the presence of the NRPS substrate phosphopantetheinylated EntB (holo-EntB), consistent with the reported mechanism of EntE-catalyzed acyl transfer to the P-Pant group on Ser245 of EntB (*33*). Residues comprising the obligate EntE−holo-EntB interaction interface have been identified through mutagenic studies (*31*). We have recently reported that EntE can also efficiently interact with EntB prior to its phosphopantetheinylation (i.e., as apo-EntB). We showed that formation of the EntE−apo-EntB complex is optimal in the presence of exogenous DHB, and that the interaction was of relatively low affinity ($EC_{50} \sim 1.5$ μM) (*32*). The EntE−apo-EntB−DHB complex is likely regulatory in nature and is thus distinct from the EntE−holo-EntB NRPS obligate complex. Residues involved in the interaction interface of the obligate interaction of acyl-holo-EntB with the NRPS substrate holo-EntF have also been reported (*22*).

The enzymes EntA and EntE are found at the interface of the two major segments of enterobactin biosynthesis. EntA (EC 1.3.1.28) catalyzes the final reaction in the DHB synthesis segment (Scheme 1B). EntA has a subunit molecular mass of 26249 Da (*17*). The EntA crystal structure revealed EntA to be tetrameric, being composed of a dimer of dimers (*34*). EntE (EC 2.7.7.58) catalyzes the first reaction in the NRPS segment by activating DHB, the product of EntA, through ATP-dependent adenylation (Scheme 1C). EntE has a subunit molecular mass of 59112 Da and is monomeric, being a member of the adenylate-forming family of enzymes (*35*−*38*). This enzyme catalyzes the adenylation of DHB, as well as its attachment in the activated form to the phosphopantetheine moiety of the downstream NRPS substrate holo-EntB. The EntE catalytic mechanism has been elucidated in a recent report showing that EntE catalyzes two half-reactions in a bi-uni−uni-bi ping-pong mechanism. (i) In the first half-reaction, DHB binds to EntE followed by the cosubstrate ATP. DHB is then adenylated followed by release of pyrophosphate (PP_i). (ii) In the second half-reaction, the EntE−DHB−AMP complex binds to holo-EntB, resulting in the transfer of DHB to the phosphopantetheine group on Ser245 of EntB, resulting in the production of acyl-holo-EntB; this is followed by release of AMP from EntE (*39*). Interestingly, it has also shown that in the absence of holo-EntB, EntE catalyzes the slow production of P^1,P^3-diadenosine 5′-tetraphosphate (Ap4A), a molecule that is involved in the modulation of cellular stress (*40*). This highlights not only the importance of the EntE−holo-EntB obligate interaction during normal enterobactin biosynthesis but also a potential protective role for EntE when it is expressed in the absence of EntB.

Here we report the first evidence of a protein−protein interaction between the sequentially related enzymes EntA and EntE, thus establishing a direct, physical link between the DHB synthesis and NRPS segments of enterobactin biosynthesis. Through the use of various in vitro assays, we show that EntA and EntE specifically interact to form a protein−protein complex. The nature of this interaction appears to be significantly affected by the oligomeric structure of EntA, which undergoes a concentration-dependent transition from dimer to tetramer at low micromolar concentrations. We report here that the EntA−EntE interaction also results in stimulation of EntE activity, likely through a conformational remodeling of the EntE active site, such that EntA exerts an activating role in the first half-reaction (DHB adenylation). EntE catalysis of DHB adenylation therefore appears to be optimized when the enzyme is assembled into a complex with EntA during enterobactin biosynthesis. The discoveries reported here further highlight the integral role of protein−protein interactions in networking the enterobactin biosynthetic pathway.

EXPERIMENTAL PROCEDURES

Reagents. Most reagents were purchased from Bioshop Canada, Inc. (Burlington, ON). 2,3-Dihydroxybenzoic acid (DHB) was purchased from Sigma-Aldrich (St. Louis, MO). Inorganic pyrophosphatase was purchased from Invitrogen (Carlsbad, CA).

Protein Expression and Purification. Hexahistidine-tagged EntA and EntE were purified from *E. coli* AG-1 cells [obtained from the ASKA repository (*41*)] harboring appropriate pCA24N-based expression constructs. Each protein was expressed with an in-frame hexahistidine tag and spacer region at the N-terminus (MRGSHHHHHHTDPALRA...), and a short extension at the C-terminus (...GLCGR[STOP]). Recombinant EntA and EntE were overexpressed and purified using immobilized metal affinity chromatography as reported previously (*32*). In this study, all protein concentrations were determined by measuring absorbance at 280 nm and using molar extinction coefficients predicted from primary amino acid sequences (ε = 57300 and 20970 M^{-1} cm^{-1} for EntE and EntA, respectively). Protein concentrations are reported as concentrations of the monomer subunit unless otherwise indicated.

Analytical Ultracentrifugation. Sedimentation velocity experiments were performed in a Beckman XL-I analytical ultracentrifuge with a four-place An-60Ti rotor. Runs were initiated after extensive thermal equilibration (> 5 h) of the rotor and sample-containing cells at 20 °C. Solutions containing 50 mM Tris (pH 7.5), 150 mM NaCl, 0.5 mM TCEP, and varying concentrations of EntA or EntE were centrifuged at 40000 rpm over approximately 10 h. A total of 250 absorbance scans were collected per run in which the optical density at 280 nm was measured. Sedimentation velocity data were fit to $g(s^*)$ and $g^\wedge(s^*)$ distributions using DCDT+ (version 2.2.1) (*42*). A number of scans (~17 scans per analysis; $\omega^2 t$ intervals all roughly between 10×10^{-10} and 16×10^{-10} rad^2/s) from each run were selected such that the peak broadening limit was always between ~150 and 160 kDa. Fits to $g(s^*)$ distributions were used for qualitative graphical comparison of concentration-dependent sedimentation behavior. Fits of $g^\wedge(s^*)$ distributions (in which concentration distributions were not based on zero-time extrapolations) were

used to quantitatively determine weight-average sedimentation coefficients. SEDPHAT (*43*) was used for global analysis of concentration-dependent EntA oligomerization. SEDPHAT global analysis was performed using four sedimentation velocity runs (EntA at 2, 4, 8, and 18 μM; 250 scans per run). The data were fit to the monomer−dimer self-association model of SEDPHAT, in which the EntA dimer was modeled as the "monomer"' and the EntA tetramer was modeled as the "dimer", assuming that the EntA dimer sedimented as a stable nondissociating species over the concentration range examined, consistent with the reported EntA crystal structure in which EntA subunits are arranged as a dimer of dimers (*34*). Estimations of $S_{20,W}$ values for the EntA dimer and EntA tetramer, which are required in the SEDPHAT global analysis, were obtained by hydrodynamic bead modeling using HYDROPRO (*44*) with the EntA Protein Data Bank (PDB) structure (2FWM) as input (either all four chains of the tetrameric biological assembly or the two chains from the structure that comprise the physiological dimer). The fit to the SEDPHAT self-association model was optimized using both simplex and Marquardt−Levenberg algorithms. For both DCDT+ and SEDPHAT analyses, SEDNTERP (version 1.09) (*45*) was used as appropriate for estimation of the following parameters at 20 °C: solution viscosity, solution density, and protein partial specific volume (as predicted from the primary amino acid sequence).

Dynamic Light Scattering. Dynamic light scattering measurements were performed on a temperature-controlled Wyatt DynaPro Titan dynamic light scattering instrument (Protein Solutions, Charlottesville, VA) using a 12 μL quartz cuvette at 20 °C. Prior to the collection of DLS data, purified EntE and EntA samples were extensively dialyzed against a buffer containing 50 mM Tris (pH 8.0), 150 mM NaCl, and 0.5 mM TCEP. Proteins were briefly centrifuged at 21000*g* immediately prior to data acquisition to remove any particulate matter or insoluble aggregates. Light scattering was measured at a wavelength of 831.15 nm and an angle of 90°. For each protein sample measurement, data were collected for at least 50 acquisitions with a 10 s averaging time per acquisition. Three independent measurements were taken for each protein sample such that the values reported are average values with accompanying standard deviations. Light scattering data were analyzed using Dynamics (version 6.12).

Pull-Down Assays. The ProFound Pull-Down PolyHis Protein:Protein Interaction Kit (Pierce, Rockford, IL) was used to study in situ interactions formed between hexahistidine-tagged recombinant bait proteins (EntA and EntE) and chromosomally expressed prey proteins from *E. coli* lysates in the presence or absence of exogenous DHB (100 μM). Pull-down assays were performed at room temperature as described previously (*32*). Bait proteins and coeluting proteins were recovered and separated on 10% SDS−polyacrylamide gels. Proteins in bands excised from the gel were trypsinized and analyzed by LC−MS/MS at the McGill Mass Spectrometry Core Facility (McGill University, Montreal, QC) as described previously (*32*).

Chemical Cross-Linking. Recombinant proteins were covalently cross-linked using the Controlled Protein−protein Cross-linking Kit (Pierce). In a typical cross-linking reaction, EntA was dialyzed against phosphate-buffered saline (pH 7.2) and then incubated with a 50-fold molar excess of the heterobifunctional cross-linker sulfo-SMCC for 30 min at room temperature. Purified maleimide-activated EntA-SMCC conjugate (22 μM) was then incubated with purified EntE (2.5 μM) for 60 min at room temperature. Cross-linking reaction mixtures were concentrated using Microcon YM-30 centrifugal filter units (Millipore). Concentrated proteins were then denatured and separated on a 10% SDS−polyacrylamide gel. Peptides recovered from bands containing cross-linked proteins were analyzed by LC−MS/MS as described above. As a control, maleimide-activated BSA was prepared as described above and mixed with purified EntE; proteins were then resolved on a 10% SDS−polyacrylamide gel.

Enzyme Activity Assays. A pyrophosphate release assay adapted from ref *35* was used to monitor the effect of EntA on EntE activity. Reaction mixtures (total volume of 100 μL) containing EntE (1 μM) and EntA (0.25 and 4 μM), 0.2 unit of *E. coli* inorganic pyrophosphatase, 75 mM Tris (pH 8.0), 10 mM $MgCl_2$, 5 mM ATP, 5 mM DTT, and 2 mM salicylate were incubated at 37 °C, and aliquots were withdrawn at 30 s time intervals. The amount of inorganic phosphate produced by the coupled enzyme reactions was measured spectrophotometrically by mixture with an ammonium molybdate−malachite green solution, resulting in the formation of a chromophore that maximally absorbs at 620 nm (*46*). A control experiment was also performed in which EntE activity was assayed as described above, but in the presence of 4 μM bovine serum albumin instead of EntA. Additionally, EntA (4 μM) was assayed in the absence of EntE to determine if our EntA preparation contained any residual activities that could result in pyrophosphate formation. EntE initial velocities were measured as the production of inorganic pyrophosphate as a function of time.

Fluorescence Spectroscopy. Fluorescence emission spectra (λ_{ex} = 280 nm) were recorded at 20 °C using a Shimadzu RF-5301PC spectrofluorimeter. Solutions of EntE (3 μM) and DHB (60 μM) in buffer A [50 mM Hepes (pH 8.0), 1.0 mM TCEP, and 15% glycerol] with or without EntA (3 μM) were supplemented with KCl to a final concentration of either 100 or 300 mM. Slit widths (excitation and emission) were set to 3 nm. Each spectrum presented is the average of three scans. Fluorescence emission data were corrected for background, dilution, and inner-filter effects as appropriate.

Fluorescence Anisotropy. Fluorescence anisotropy measurements were performed on a Varian Cary Eclipse spectrofluorimeter equipped with automated polarizers. Measurements were taken for solutions containing buffer A and 100 mM KCl supplemented with various combinations of DHB (20 μM), EntA (15 μM), and EntE (7 μM). Measurements of DHB fluorescence anisotropy in the presence and absence of proteins were taken in triplicate at 20 °C at wavelengths of maximal DHB excitation and emission (310 and 440 nm, respectively). Anisotropy (r) values were calculated according to the following equation (adapted from ref *47*):

$$r = (I_{VV} - I_{VH})/(I_{VV} + 2I_{VH}) \quad (1)$$

where I_{VV} is the fluorescence emission intensity read at 440 nm with polarizers positioned in a parallel orientation and I_{VH} is the fluorescence emission intensity read at 440 nm with the polarizers in a perpendicular orientation.

Fluorescence-Based Equilibrium Binding Assay. The DHB−EntE FRET signal (*32*) of solutions containing buffer A with 100 mM KCl, 3 μM EntE, 60 μM DHB, and varying concentrations of EntA (0.5−7 μM) was measured as the fluorescence emission intensity of the solution monitored at 440 nm upon excitation at 280 nm. Fluorescence emission data were recorded at 20 °C using a Varian Cary Eclipse spectrofluorimeter

equipped with a Peltier temperature controller. Fluorescence emission intensities were corrected for inner-filter effects, dilutions, and background. To analyze equilibrium binding data collected in these experiments, $[EntA]_{bound}$ and $[EntA]_{free}$ at a given $[EntA]_{total}$ were calculated from changes in EntE-bound DHB fluorescence emission intensity (ΔF) measured at 440 nm in the presence of varying concentrations of EntA:

$$\Delta F = F_0 - F \quad (2)$$

where F_0 is the corrected fluorescence emission intensity of DHB bound to EntE in the absence of EntA and F is the corrected fluorescence emission intensity of DHB bound to EntE at a given EntA concentration.

Binding assays were performed in triplicate to determine mean values for changes in fluorescence intensity as a function of EntA concentration. To normalize for slight variations in F_0 between replicates, we expressed the change in fluorescence intensity ($\Delta F/F_0$) at a given $[EntA]_{total}$ by dividing this value by the maximal change in fluorescence intensity observed in a given replicate at a saturating concentration of EntA [$(\Delta F/F_0)_{max}$]. We define the resulting ratio as fractional binding: $(\Delta F/F_0)/(\Delta F/F_0)_{max}$, where $(\Delta F/F_0)_{max}$ was obtained by plotting $\Delta F/F_0$ as a function of $[EntA]_{total}$ and fitting the plotted data to the equation describing a dose−response curve in Origin version 8.1 (OriginLab Corp., Northampton, MA); the curve maxima obtained from these fits were used to determine $(\Delta F/F_0)_{max}$. We used fractional binding to directly relate the observed decrease in DHB fluorescence emission at 440 nm to the fraction of EntE in complex with EntA, as shown below:

$$[EntA]_{bound} = [EntE]_{bound} = [EntE]_{total} \times (\Delta F/F_0)/(\Delta F/F_0)_{max} \quad (3)$$

In all fluorescence titration experiments in this study, $[EntE]_{total}$ was 3 μM. Because $[EntA]_{total}$ was experimentally determined by measuring OD_{280}, we derived the concentration of EntA in the free fraction as follows:

$$[EntA]_{free} = [EntA]_{total} - [EntA]_{bound} \quad (4)$$

Equilibrium binding data were fit to the Hill equation:

$$(\Delta F/F_0)/(\Delta F/F_0)_{max} = [EntA]_{free}^{n_H}/(K_{0.5}^{n_H} + [EntA]_{free}^{n_H}) \quad (5)$$

where n_H is the Hill coefficient and $K_{0.5}$ is the concentration of $[EntA]_{free}$ at which 50% binding is observed. Nonlinear fits of equilibrium binding data to the Hill equation were performed using Origin version 8.1.

Isothermal Titration Calorimetry. Calorimetric titrations were conducted using a VP-ITC isothermal titration microcalorimeter from MicroCal, Inc. (Piscataway, NJ). Calorimetry experiments were performed at 10 °C to minimize protein aggregation caused by mechanical stirring. Initial concentrations in the cell and syringe were as follows: 10 μM EntA and 170 μM EntE, respectively. For ITC experiments, proteins were first extensively dialyzed against a buffer containing 50 mM Hepes (pH 8.0), 100 mM KCl, 1.0 mM TCEP, and 15% glycerol. A total of 28 injections with a 10 μL injection volume were made at 240 s intervals. An initial injection with a 4 μL volume was included to ensure accurate volume delivery from the syringe, and the heat generated from this injection was not included in the data analysis. The final three injections displayed constant heat evolution indicative of saturation of EntA binding sites for EntE, and the integrated heats of these injections were averaged and taken as the heat of dilution of EntE upon injection into the cell. This averaged heat of EntE dilution was subtracted from integrated heats evolved from EntA−EntE interaction to yield corrected and normalized heat increments, which were then fit to models describing either one-site or two-site binding. Fits were refined by successive iterations until no further decreases in the χ^2 values of the fits were observed. Data were analyzed using Origin version 5.0 (Microcal).

RESULTS

Protein Expression and Purification. Preparations of recombinant, hexahistidine-tagged EntA and EntE were each expressed in *E. coli* AG-1 cells and purified by a single IMAC affinity chromatography step. The purity of proteins eluted from the IMAC columns was assessed by SDS−polyacrylamide gel electrophoresis and found to be nearly homogeneous (purity of > 95%). Yields obtained were typically in the range of 20−30 mg of purified protein/L of culture.

Analytical Ultracentrifugation. We performed sedimentation velocity analytical ultracentrifugation (AUC) experiments on solutions of purified EntA and EntE to gain insights into the oligomeric state of these proteins as a function of concentration. We used DCDT+ to perform model-independent, time-derivative $g(s^*)$ analyses of our sedimentation velocity data, resulting in a graphical representation of the abundance of sedimenting species as a function of $S_{20,W}$ (Figure 1). We observed that EntE consistently sedimented as a monomer with an $S_{20,W}$ value of approximately 4.0, independent of EntE concentration between 2.5 and 13 μM (Figure 1A). In contrast, large changes in EntA sedimentation behavior were observed upon alteration of the EntA concentration. Over a concentration range from 2 to 18 μM, EntA sedimented as a single peak, but that peak position shifted significantly with an increasing concentration (Figure 1B). Concentration-dependent changes in sedimentation coefficients of sedimenting species are indicative of reversible self-association occurring between sedimenting species during the AUC experiment. In such a situation, the $g(s^*)$ distribution reflects an average reaction boundary of the reversible association and not to discrete sedimenting species (*48*). We used the $g^\wedge(s^*)$ analysis function of DCDT+ to quantitatively determine $S_{20,W}$ values for EntE and EntA at different concentrations (Table 1). Consistent with our $g(s^*)$ analyses, the $S_{20,W}$ of EntE did not change significantly over the concentration range examined (Table 1, rows 1−3). The EntA $S_{20,W}$ increased from 3.87 ± 0.35 at a total loading concentration of 2 μM to 5.70 ± 0.09 at 18 μM (Table 1, rows 4−7). A plot (not shown) of EntA $S_{20,W}$ versus loading concentration revealed that the sedimentation coefficients followed a hyperbola-like trend with EntA concentration, indicative of self-association over the observed concentration range. We used SEDPHAT to assess the fit of our sedimentation velocity data to a model describing dimer−tetramer self-association [given that the EntA sedimenting species at 2 μM had an $S_{20,W}$ similar to that of the 60 kDa EntE monomer and that EntA also adopts a globular fold, we concluded that at this concentration EntA was predominantly in the dimeric (57.2 kDa) form]. For SEDPHAT global analysis, we required sedimentation coefficients for the EntA dimer and EntA tetramer. Because our sedimentation

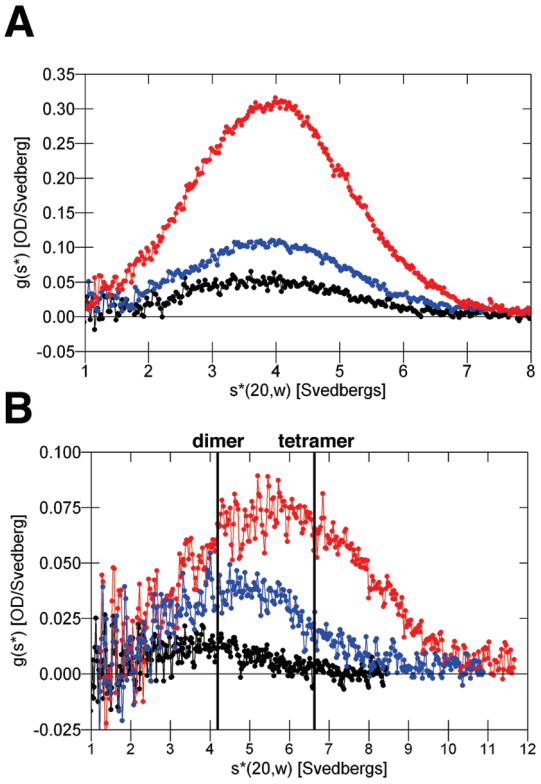

FIGURE 1: Sedimentation velocity analytical ultracentrifugation of EntE and EntA. (A) $g(s^*)$ distributions fit to sedimentation velocity data obtained at 20 °C from EntE solutions at the following concentrations: 2.5 μM (black circles), 4.5 μM (blue circles), and 13 μM (red circles). (B) $g(s^*)$ distributions fit to sedimentation velocity data obtained at 20 °C from EntA solutions at the following concentrations: 2 μM (black circles), 8 μM (blue circles), and 18 μM (red circles). For the sake of clarity, the $g(s^*)$ distribution of EntA at 4 μM is not shown in this figure, but the $S_{20,W}$ for EntA at this concentration is reported in Table 1. The left vertical line represents the $S_{20,W}$ of dimeric EntA calculated with HYDROPRO. The right vertical line represents the $S_{20,W}$ of tetrameric EntA calculated with HYDROPRO.

Table 1: Sedimentation Velocity Analytical Ultracentrifugation of Purified EntE and EntA

protein	concn[a] (μM)	$S_{20,W}$[b]	c/c_{tot}[c]	rmsd[d]
EntE	2.5	3.93 ± 0.17	0.859	not applicable
EntE	4.5	4.04 ± 0.07	0.879	not applicable
EntE	13.0	3.93 ± 0.04	0.869	not applicable
EntA	2.0	3.87 ± 0.35	0.866	0.01057
EntA	4.0	4.48 ± 0.23	0.869	0.01054
EntA	8.0	4.97 ± 0.15	0.883	0.01077
EntA	18.0	5.70 ± 0.09	0.864	0.01553

[a]Protein concentration determined by A_{280} and expressed as a micromolar concentration of monomer subunits. [b]Weight-average sedimentation coefficients determined by fits to $g^\wedge(s^*)$ distributions using DCDT+. Standard errors to fits also given. [c]Ratio of the absorbance contribution of sedimenting species identified by $g^\wedge(s^*)$ analysis to total absorbance in the cell. [d]Local root-mean-square deviations of fits to the self-association model using SEDPHAT global analysis.

velocity data indicated that our samples contained mixtures of EntA dimer and tetramer over the concentration range examined, we could not experimentally determine sedimentation coefficients for discrete EntA dimer or tetramer. We therefore employed hydrodynamic bead modeling using HYDROPRO, with the published X-ray crystallographic structure of EntA (PDB entry 2FWM) as input. According to our HYDROPRO analyses, the EntA dimer was predicted to have an $S_{20,W}$ value of 4.23 and the EntA tetramer to have an $S_{20,W}$ value of 6.71. These positions are shown in Figure 1B as vertical lines. The HYDROPRO-predicted $S_{20,W}$ of the EntA dimer is consistent with our experimental $S_{20,W}$ of EntA determined by $g^\wedge(s^*)$ analysis at the lowest concentration that we examined (2 μM), indicating that EntA is mostly a dimer at this concentration. At the upper boundary of our concentration range (18 μM), our experimentally derived $S_{20,W}$ value of 5.70 is significantly lower than that predicted for the homogeneous EntA tetramer, suggesting that at this concentration EntA was present as both dimers and tetramers, with the majority of the protein being in the tetrameric form. Sedimentation velocity data from the four runs (250 absorbance scans per run) recorded between 2 and 18 μM EntA fit well to the SEDPHAT monomer−dimer self-association model (here the EntA dimer was modeled as a monomer and the EntA tetramer as a dimer, assuming no dissociation of dimer to monomer over this concentration range). The reduced χ^2 value of the global fit was 1.46, which is acceptable given that a χ^2 value of 1.00 in SEDPHAT global analysis represents a perfect fit to the model (*43*). The root-mean-square deviations of fits of local data sets to the global SEDPHAT self-association model were also found to be acceptable [each root-mean-square deviation (rmsd) was less than 0.016 (Table 1, column 5)]. The K_D of the EntA dimer−tetramer equilibrium was determined by SEDPHAT global analysis to be 12.30 μM (or 6.15 μM if total EntA is expressed as dimer equivalents).

Dynamic Light Scattering. We performed dynamic light scattering (DLS) experiments at 20 °C to further investigate the oligomeric structures of EntE (12 μM) and EntA (4 and 9 μM) in solution (Table 2). We found that EntE had an average hydrodynamic radius of 3.6 ± 0.1 nm with an apparent molecular mass of 66.0 ± 3.6 kDa (Table 2, row 1), consistent with our AUC data that showed that EntE exists in solution as a monomer with a sequence-predicted molecular mass of 60 kDa. EntE hydrodynamic behavior did not change as a function of protein concentration. At 24 μM, EntE was still observed to have a hydrodynamic radius of 3.5 nm and an apparent molecular mass of 65 kDa. In contrast, our DLS data, consistent with our AUC results, showed that EntA hydrodynamic behavior was concentration-dependent. At 4 μM, EntA in solution was observed to have an average hydrodynamic radius of 3.7 ± 0.1 nm and an apparent molecular mass of 72.7 ± 8.6 kDa (Table 2, row 2). At 9 μM, EntA in solution was observed to have an average hydrodynamic radius of 4.1 ± 0.1 nm and an apparent molecular mass of 92.0 ± 2.6 kDa (Table 2, row 3). The molecular masses determined by DLS for EntA lie between its predicted size as a dimer (57.2 kDa) and as a tetramer (114.4 kDa); at the lower concentration, the apparent molecular mass is closer to the predicted dimer size, while at the higher concentration, there is a shift in the apparent molecular mass toward the predicted tetramer size. These results agree with our AUC data showing that EntA is a mixture of dimers and tetramers in this concentration range undergoing rapid equilibrium between these oligomeric states. In both our AUC and DLS experiments, we observed an averaged species reflecting rapid dimer−tetramer self-association.

Pull-Down Assays. We previously showed that recombinant EntB when used as a bait protein could pull down chromosomally expressed EntE from *E. coli* lysates and further that pull-down efficiency increased substantially in the presence of exogenous DHB (*32*). Here we used purified, recombinant EntE and

Table 2: Dynamic Light Scattering by EntE and EntA in Solution

protein	R_H[a] (nm)	molecular mass (kDa)	polydispersity (%)	mass contribution[b] (%)
EntE[c]	3.6 ± 0.1	66.0 ± 3.6	9.5 ± 2.6	99.1 ± 0.2
EntA (4 μM)	3.7 ± 0.2	72.7 ± 8.6	10.6 ± 2.9	98.4 ± 0.1
EntA (9 μM)	4.1 ± 0.1	92.0 ± 2.6	11.8 ± 3.0	97.1 ± 0.6

[a]Hydrodynamic radius. [b]Contribution of scattering species to the total mass of scattering species in the experiment. [c]EntE concentration of 12 μM.

EntA bait proteins in pull-down experiments to identify respective binding partners from lysates of iron-starved *E. coli* cells in the presence and absence of exogenous DHB. Bait proteins were immobilized to Co^{2+}-chelate beads and then incubated with lysates from *E. coli* BW25113 cells grown under iron-restricted conditions (M63 minimal medium with 75 μM 2,2′-dipyridyl), resulting in expression of the enterobactin biosynthetic machinery by derepression of Fur. We initially used EntA as a bait protein to determine what partner proteins could be pulled down from *E. coli* cell lysates in the presence and absence of DHB (Figure 2A). We found that EntA bait was able to pull down a protein migrating at approximately 60 kDa by SDS−PAGE analysis independent of whether exogenous DHB (100 μM) was added to the cell lysate (Figure 2A, band a, −DHB and +DHB, respectively). Trypsinized proteins recovered from these bands were analyzed by LC−MS/MS, and the recovered peptides were found to correspond to *E. coli* EntE (Table S1 of the Supporting Information, rows 1−41). The bands visible above the a (−DHB and +DHB) bands were also present in a control experiment (in which the lysate was applied to the empty column) and therefore do not represent a prey protein that specifically binds to EntA (data not shown). In a second pull-down experiment, we used EntE as a bait protein to pull down partner proteins from iron-restricted *E. coli* cell lysates with or without exogenously added DHB (Figure 2B). EntE bait was also able to pull down a protein migrating at approximately 30 kDa (Figure 2B, band d, +DHB) that was determined by LC−MS/MS to be *E. coli* EntB (Table S1 of the Supporting Information, rows 42−57). This band was observed only when exogenous 2,3-DHB was added to the lysate prior to equilibration with immobilized EntE bait. We also found that EntE pulled down in a DHB-independent manner a protein migrating at approximately 26 kDa (Figure 2B, band e, −DHB and +DHB, respectively). Mass spectrometry of proteins extracted from the e (−DHB) and e (+DHB) bands confirmed that they contained peptides corresponding to *E. coli* EntA (Table S1 of the Supporting Information, rows 58−78).

Chemical Cross-Linking. A solution of EntA was incubated with the heterobifunctional cross-linker SMCC, resulting in covalent attachment of the *n*-hydroxysuccinimide moiety of the cross-linker to primary amines on EntA. Maleimide-activated EntA (22 μM) was then mixed with a solution of EntE (2.5 μM) to form cross-links between EntE cysteine residues and the EntA-SMCC conjugate. Resolution of cross-linked products on an SDS−polyacrylamide gel revealed the presence of a single band corresponding to a large (> 250 kDa) complex in addition to bands corresponding to un-cross-linked EntA and EntE. This additional band was observed in the presence of SMCC, but not in the absence of SMCC (Figure S1 of the Supporting Information). The size of the +SMCC band is consistent with a cross-linked product containing four EntE monomers and four EntA monomers. Analysis of tryptic peptides from proteins recovered from the > 250 kDa band revealed that it contained both *E. coli* EntA and EntE sequences (Table S2 of the Supporting Information),

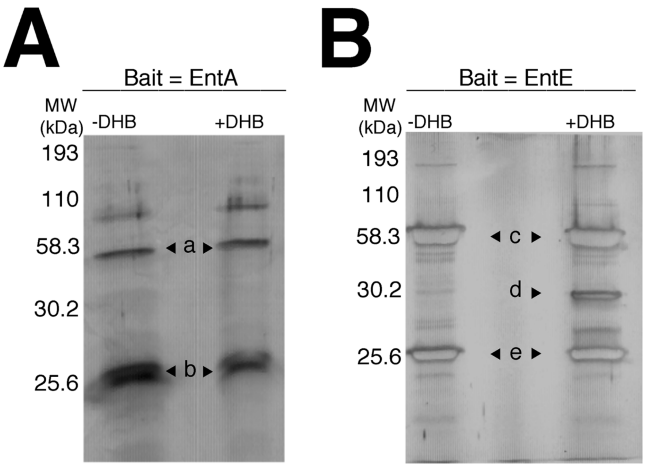

FIGURE 2: Pull-down assays of EntA−EntE and EntE−EntB complexes formed in situ. (A) Silver-stained 10% SDS−polyacrylamide gel of *E. coli* proteins coeluted from Co^{2+}-chelate beads when EntA was used as bait. (B) Same as panel A, but with EntE being used as bait. Lane −DHB contained proteins eluted from beads exposed to the iron-restricted *E. coli* BW25113 lysate in the absence of exogenous DHB. Lane +DHB contained proteins eluted from the beads exposed to the iron-restricted *E. coli* BW25113 lysate in the presence of exogenous DHB (100 μM). Positions of migration of protein molecular mass standards (Kaleidoscope Pre-Stained Markers, Bio-Rad Laboratories) are shown at the left of each gel. Labels a−e indicate bands in which proteins were extracted and identified by LC−MS/MS: (a) *E. coli* EntE from lysate, (b) EntA (bait), (c) EntE (bait), (d) *E. coli* EntB from lysate, and (e) *E. coli* EntA from lysate. Peptide sequences identified by LC−MS/MS for recovered chromosomally expressed *E. coli* prey proteins are listed in Table S1 of the Supporting Information.

confirming that this band represented a cross-linked EntA−EntE complex. A control reaction in which maleimide-activated BSA was mixed with EntE was also performed, and no cross-linked species were observed, indicating the specificity of the EntA−EntE cross-linked product (Figure S2 of the Supporting Information).

EntE Activity Assays. Because we found that EntE can form a complex with EntA, we were interested in determining the effect of EntA interaction on EntE activity. It was previously reported that the level of adenylation of DHB by EntE increased approximately 10-fold in the presence of the NRPS substrate holo-EntB (*33*), a consequence of this obligate protein−protein interaction. Could a similar increase in EntE activity also occur in the presence of the protein (EntA) that produces the DHB substrate used by EntE? Here we found that addition of purified EntA at concentrations of 0.25 and 4 μM to a solution containing 1 μM purified EntE resulted in 3-fold [Figure 3 (▼)] and 6-fold [Figure 3 (▲)] increases in EntE initial velocity, respectively, relative to the initial velocity of EntE-catalyzed production of pyrophosphate product in the absence of EntA [Figure 3 (■)]. We did not observe any significant change in EntE activity upon the addition of a control protein, bovine serum albumin at a concentration of 4 μM

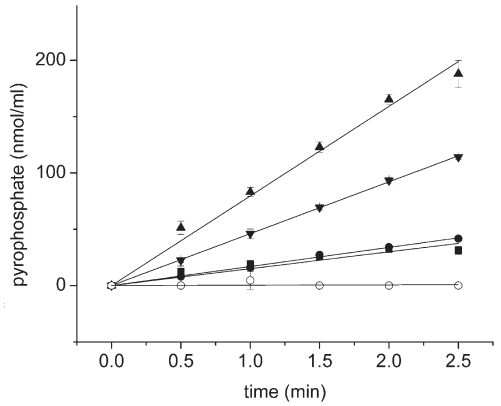

FIGURE 3: Stimulation of EntE activity by EntA. Initial velocities of EntE (—) fit to the production of pyrophosphate as a function of time: EntE alone (■), EntE and 0.25 μM EntA (▼), EntE and 4 μM EntA (▲), EntE and 4 μM bovine serum albumin (●), and EntA (4 μM) in the absence of EntE (○). Data shown are averaged values of triplicate readings. Error bars represent the standard deviation from averaged values.

[Figure 3 (●)], demonstrating that the observed increase in EntE activity was specific to EntA. Furthermore, a control assay with 4 μM EntA performed in the absence of EntE resulted in the production of no pyrophosphate [Figure 3 (○)], indicating the presence of no contaminating activities in our EntA preparation that could contribute to the observed EntA-dependent increases in pyrophosphate production observed in our assays.

Effect of EntA on the EntE−DHB FRET Signal. The observed stimulatory effect of EntA on EntE activity led us to investigate if conformational changes at the EntE active site did indeed occur upon formation of the EntA−EntE complex. We used fluorescence spectroscopy to further investigate the EntA−EntE interaction by observing the effect of EntA on the EntE−DHB FRET signal that we reported previously (*32*). The corrected fluorescence emission spectrum of the EntE (3 μM)/DHB (60 μM) solution containing 100 mM KCl in the absence of EntA is shown in Figure 4 (---). The maximum at 440 nm corresponds to DHB fluorescence emission upon excitation of EntE intrinsic fluorophores at 280 nm. When the experiment was repeated with the addition of 3 μM EntA, the observed corrected spectrum exhibited a 1.75-fold decrease in the peak maximum at 440 nm [Figure 4 (—)]. We performed a similar experiment with EntA present but increased the concentration of KCl from 100 to 300 mM [Figure 4 (···)]. We found that this increase in ionic strength almost restored the EntE−DHB FRET signal to its initial intensity, even in the presence of EntA. We did not observe any KCl-dependent effect on the EntE−DHB FRET signal in the absence of EntA. This specificity suggests that the restoration of the FRET signal at 300 mM KCl is due to a salt-dependent disruption of an EntA−EntE complex.

Fluorescence Anisotropy Experiments. To determine the binding status of DHB during EntA−EntE interaction, we measured the fluorescence anisotropy of DHB in the absence and presence of EntA and/or EntE. We observed that in the absence of protein, the fluorescence anisotropy (r) of DHB at a concentration of 20 μM was near zero, indicating a rapid rate of rotational diffusion in solution [Figure 5 (black bar)]. The addition of 15 μM EntA to the DHB solution did not result in a significant increase in DHB anisotropy [Figure 5 (dark gray bar)]. The addition of EntE (7 μM) to DHB results in a relatively large increase in DHB anisotropy, consistent with its ability to bind DHB as a substrate

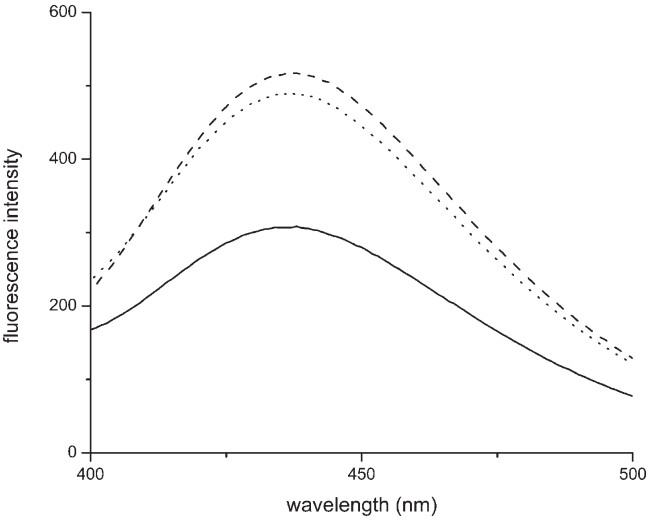

FIGURE 4: Perturbation of the DHB−EntE FRET signal by EntA. Fluorescence emission spectra recorded at 20 °C show DHB fluorescence emission around 440 nm upon excitation of mixtures of DHB with EntE with or without EntA at 280 nm: 3 μM EntE and 60 μM DHB (---); 3 μM EntE, 60 μM DHB, and 3 μM EntA in a buffer containing 100 mM KCl (—); and 3 μM EntE, 60 μM DHB, and 3 μM EntA in a buffer containing 300 mM KCl (···).

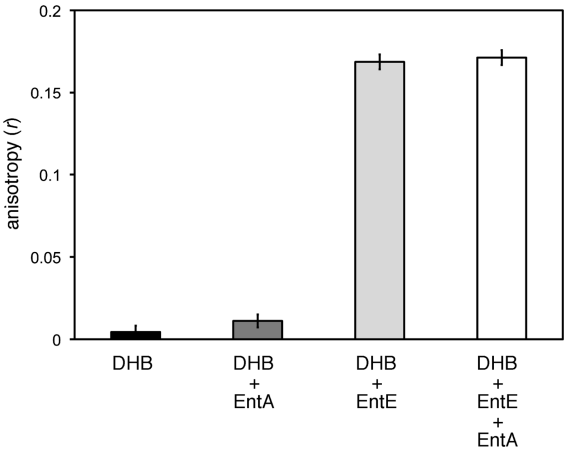

FIGURE 5: Fluorescence anisotropy of DHB. Fluorescence anisotropy measurements (λ_{ex} = 310 nm; λ_{em} = 440 nm) taken at 20 °C of DHB alone and in the presence of EntE and/or EntA: 20 μM DHB (black bar), 20 μM DHB and 15 μM EntA (dark gray bar), 20 μM DHB and 7 μM EntE (light gray bar), and 20 μM DHB, 15 μM EntA, and 7 μM EntE (white bar).

[Figure 5 (light gray bar)]. The addition of both EntA (15 μM) and EntE (7 μM) [Figure 5 (white bar)] resulted in the observed DHB anisotropy similar to that of DHB with EntE, showing that binding of EntA to EntE does not cause dissociation of DHB from EntE. Consistent with the short fluorescence lifetime of DHB [0.375 ns (*49*)], no additional increase in anisotropy was observed with the addition of EntA.

Fluorescence-Based Equilibrium Binding Assay. Having found that the change in the EntE−DHB FRET signal by EntA was due to the EntA−EntE interaction, we followed the decrease in this signal as a function of EntA concentration to measure the equilibrium binding behavior of formation of the EntA−EntE complex. By varying the concentration of EntA relative to a fixed concentration of EntE and DHB, we found that EntA was able to decrease the magnitude of the EntE−DHB FRET signal in a saturable, concentration-dependent manner. At 20 °C, the decrease

in the magnitude of the FRET signal was initially shallow followed by a transition to a steeper decrease commencing at an EntA concentration of approximately 4 μM (Figure 6A). We used our SEDPHAT-derived equilibrium association constant for the EntA dimer−tetramer equilibrium ($K_A = 1.63 \times 10^5\ M^{-1}$ when total EntA is expressed as dimer equivalents) to estimate the fraction of tetrameric EntA at a given $[EntA]_{total}$. The following equation, adapted from Cole (*50*), was used to relate the concentration of the EntA dimer at a given $[EntA]_{total}$ (here expressed as dimer equivalents):

$$[EntA]_{dimer} = [-1 + (1+8K_A[EntA]_{total_{as}dimer})^{1/2}]/4K_A \quad (6)$$

We were thus able to estimate at each EntA concentration used in our fluorescence-based equilibrium binding assay the fraction of EntA occurring in the tetrameric form (Figure 6A, inset). According to these calculations, the concentration of tetrameric EntA found when $[EntA]_{total}$ is saturating (7 μM) in our fluorescence assay is ~2.8 μM (i.e., fraction of EntA as a tetramer at this concentration estimated to be 0.4), which is approximately equimolar with the fixed concentration of EntE in our binding assay (3.0 μM).

EntA-dependent changes in the DHB−EntE FRET signal were used to determine fractional binding $[(\Delta F/F_0)/(\Delta F/F_0)_{max}]$. Fractional binding values were then used to calculate $[EntA]_{bound}$ and $[EntA]_{free}$ at a given $[EntA]_{total}$ (see Experimental Procedures). At 20 °C, the observed change in fractional binding as a function of $[EntA]_{free}$ was sigmoidal in character (Figure 6B). These data fit well ($R^2 = 0.975$) to the Hill equation. The Hill coefficient (n_H) determined from the nonlinear fit was 3.66, and the $K_{0.5}$ value was determined to be 1.94 μM. A Scatchard replot of our binding data revealed a concave-down trend (Figure 6B, inset).

Isothermal Titration Calorimetry. We used isothermal titration calorimetry to directly measure the EntA−EntE interaction, thus obtaining information about the affinity (K_A), thermodynamics (ΔH and $T\Delta S$), and stoichiometry (n). Because of the precipitation of proteins upon mechanical stirring at higher temperatures, we had to perform this experiment at 10 °C. At this temperature, we were able to directly measure the EntA−EntE interaction by the generation of heat upon successive injections of a solution of 170 μM EntE into a solution of 10 μM EntA (Figure 7, top panel). The integrated heats of binding were corrected for the heat of dilution of EntE and fit using Origin version 5.0 to models describing either a single binding site or two independent binding sites. The data clearly fit best to the model describing two binding sites when compared to the single-site model fit, which is evident from refined χ^2 values (24409.0 and 61194.2, respectively). The EntA−EntE binding isotherm fit to the two independent binding sites model is shown in the bottom panel of Figure 7. Binding parameters determined for the two sites by this model are listed in Table 3. Both sites have a stoichiometry of ~1, indicating that each interaction reflects one subunit of EntE interacting with one subunit of EntA (Table 3, column 2). The largest difference between the two sites is in their respective K_A values, with site 1 having an approximately 10-fold lower affinity than site 2 (Table 3, column 3). Binding at each site was observed to be exothermic with a positive entropy component (Table 3, columns 4 and 5). To improve our understanding of the distribution of EntA dimers and tetramers present in the 10 μM EntA solution used for ITC at 10 °C, we also performed

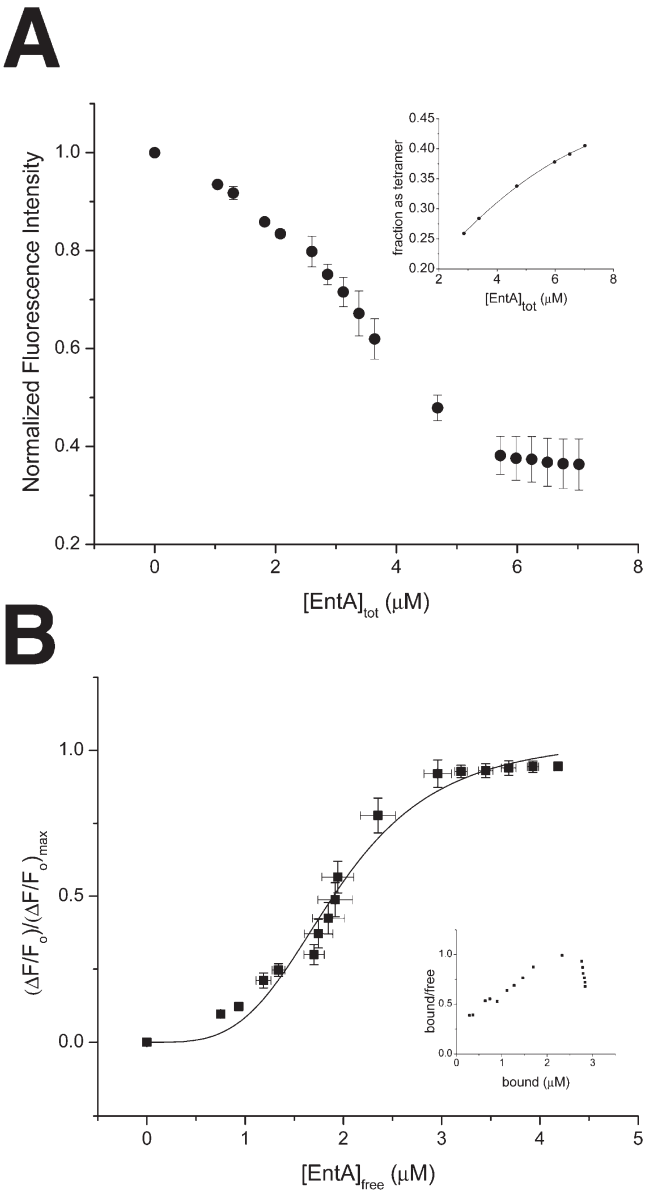

FIGURE 6: Fluorescence-based equilibrium binding assay of the EntA−EntE interaction. Binding of EntA to EntE corresponds to the decrease in the magnitude of the DHB−EntE FRET signal at 440 nm with an increasing concentration of EntA. (A) Decrease in fluorescence emission at 440 nm (λ_{ex} = 280 nm) as a function of $[EntA]_{total}$ at 20 °C (●). Data shown are averaged values of readings taken in triplicate and normalized to correct for small changes in F_0 between replicates; error bars represent standard deviations from average values. Fluorescence emission at 440 nm is due to DHB emission resulting from FRET via EntE donor residues excited at 280 nm. The inset shows an estimate of the fraction of $[EntA]_{total}$ occurring as a tetramer at concentrations used in the fluorescence assay. Fractions as tetramer were determined using the K_A of the dimer−tetramer equilibrium determined by SEDPHAT global analysis of EntA sedimentation velocity AUC data in an equation relating $[EntA]_{dimer}$ to the total loading concentration expresed as EntA dimers. Fraction as tetramer = $([EntA]_{total\_as\_dimer} - [EntA]_{dimer})/[EntA]_{total\_as\_dimer}$. The solid line represents a nonlinear fit of the data to a second-order polynomial describing eq 6 (see Results). (B) Hill plot showing the change in fractional binding $[(\Delta F/F_0)/(\Delta F/F_0)_{max}]$ as a function of $[EntA]_{free}$ (■). Error bars along the y-axis reflect standard deviations of averaged fractional binding determinations from three experiments; error bars along the x-axis reflect standard deviations of averaged $[EntA]_{free}$ determinations from three experiments. The inset shows a Scatchard replot of the same data, in which $[EntA]_{bound}$ = fractional binding × $[EntE]_{total}$. See Experimental Procedures for details about how $[EntA]_{bound}$ and $[EntA]_{free}$ were determined.

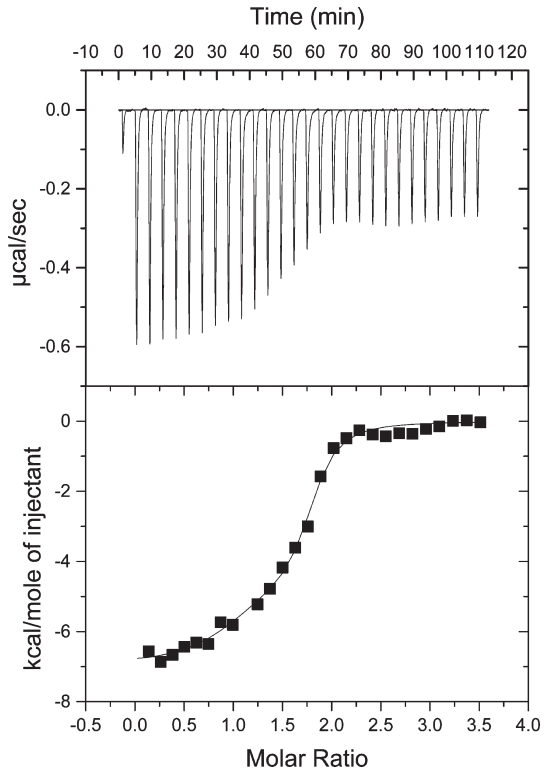

FIGURE 7: Isothermal titration calorimetry (ITC) of the EntA−EntE interaction. The top panel shows heats evolved during successive injections of a 170 μM EntE solution into a 10 μM EntA solution at 10 °C. The final three heats of injection were not observed to significantly vary and were taken to represent heats of dilution of EntE into a solution containing saturated EntA. The bottom panel shows the EntA−EntE binding isotherm determined from the integrated heats evolved during injection of EntE into the EntA solution. Black squares represent corrected and normalized evolved heat increments as a function of the EntE:EntA molar ratio at each injection. The solid line represents the best fit of heat increment data to a model describing two independent binding sites (see Table 3).

Table 3: Analysis of EntA−EntE Isothermal Titration Calorimetry Data

site[a]	n^b	$K_A{}^c$ ($\times 10^7$ M^{-1})	ΔH (kcal/mol)	$T\Delta S$ (kcal/mol)
1	0.79 ± 0.19	0.45 ± 0.12	−4.55 ± 1.20	4.08
2	0.96 ± 0.21	4.06 ± 0.78	−6.99 ± 0.40	2.89

[a]EntA−EntE isothermal titration calorimetry data collected at 10 °C were fit to a model describing two independent binding sites using Origin version 5.0. The final χ^2 value of the fit was 24409.0. Standard errors of fitted parameters are also given. [b]Stoichiometry. [c]Equilibrium association constant.

sedimentation velocity analytical ultracentrifugation experiments at 10 °C over the same EntA concentration range used at 20 °C (see Table 1, rows 4−7) and found no significant temperature-dependent differences in EntA sedimentation behavior (Table S3 of the Supporting Information). This indicates that there are no significant temperature-dependent differences in the distributions of EntA dimers and tetramers as a function of total protein concentration.

DISCUSSION

Protein−protein interactions are now known to play a key role in many metabolic processes mediated by sequential enzyme activities (*51*−*53*). Such interactions may facilitate the direct channeling of metabolic intermediates, resulting in optimization of catalysis, sequestration of intermediates to protect against diversion to other pathways, or protection against degradation of labile intermediates (*54*−*56*). The biosynthesis of the *E. coli* siderophore enterobactin is a cytoplasmic enzyme-mediated process in which protein−protein interactions are now recognized to be essential. Prior to this study, all protein−protein interactions relevant to enterobactin biosynthesis had been localized to proteins involved in the NRPS segment (EntE, EntB, EntF, and EntD) and were found to be obligate for the biosynthetic process (*22*, *30*−*32*, *57*). Here we report the first experimental evidence of a protein−protein interaction between EntA and EntE, thus establishing a direct link between the DHB synthesis and NRPS segments. Formation of an EntA−EntE complex during enterobactin biosynthesis could serve to facilitate substrate channeling, thus minimizing dissociation of DHB into the bulk medium and favoring direct, rapid entry of this intermediate into the NRPS segment. Such channeling would be advantageous because excessive accumulation of intracellular DHB during enterobactin biosynthesis in *E. coli* under iron-limiting conditions could interfere with iron uptake processes potentially requiring molecular recognition of enterobactin DHB moieties as part of their function (e.g., Fes and EntS).

In addition to facilitation of substrate channeling, we have evidence that formation of the EntA−EntE complex positively affects EntE activity. We found through our enzyme assays that EntE activity increased significantly upon addition of EntA, and in a manner dependent on EntA concentration. We propose that this stimulation of EntE activity is due to optimization of the EntE active site through conformational changes occurring upon EntA binding. Our finding that EntA perturbs the FRET signal between DHB and EntE intrinsic fluorophore donor residue(s) supports this. Formation of a complex of EntA and EntE therefore likely results in conformational changes at the EntE active site causing translocation of bound DHB toward the ATP cosubstrate and away from FRET donor residues such as Tyr236, predicted to be found at the floor of the EntE active site, consistent with the structure of the EntE homologue DhbE (*32*, *37*). Our fluorescence anisotropy experiments clearly show that DHB is not dissociated upon formation of the EntA−EntE complex, thus excluding this as an alternate explanation for the EntA-induced reduction in the magnitude of the observed FRET signal. Taken together, our data show that EntA induces a conformational remodeling of the EntE active site upon formation of the EntA−EntE complex, resulting in a repositioning of DHB within the substrate-binding cavity of EntE such that the rate of EntE-catalyzed DHB adenylation in the first half-reaction of the EntE mechanism is increased because of the proximity to ATP (Scheme 2).

We also found that the decrease in the magnitude of the DHB−EntE FRET signal was dependent on the concentration of EntA, and we exploited this phenomenon to gain insight into the equilibrium binding aspects of formation of the EntA−EntE complex. Our equilibrium binding data at 20 °C fit well to the Hill equation, with a Hill coefficient of > 1 [n_H = 3.66 (Figure 6B)]. A Hill coefficient of that magnitude, along with the concave-down behavior observed in the Scatchard replot of our binding data, suggests possible positive cooperativity in the EntA−EntE interaction (i.e., EntE affinity for EntA increases as a function of EntA concentration). Concordant with this binding behavior, our AUC data show that the oligomeric structure of EntA changes over the concentration range used in our equilibrium binding assay. We

Scheme 2: Proposed Model of the Attenuation of the EntE−DHB FRET Signal upon EntA Interaction[a]

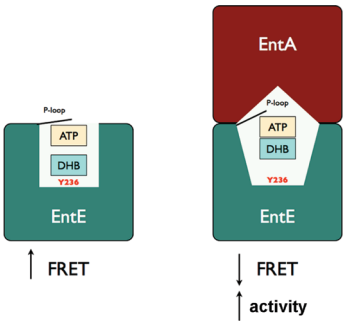

[a]EntE Y236 is shown as a putative FRET donor at the base of the EntE active site.

found that EntA exists as a mixture of dimers and tetramers at concentrations between 2 and 18 μM, with a transition from being predominantly dimer at 2 μM to being predominantly tetramer at 18 μM. The sigmoidal binding behavior observed in the EntA−EntE interaction is therefore likely caused at least in part by EntE binding with a higher affinity to EntA in the tetrameric form. However, it appears that EntE can also interact with EntA in nontetrameric forms (i.e., monomer or dimer) because we observed stimulation of EntE activity in the presence of EntA at a concentration of 0.25 μM, where the concentration of the EntA tetramer would be negligible according to our analysis of EntA self-association. That EntE binds with differential affinities to EntA depending on the EntA oligomeric state is further supported by our measurement of the EntA−EntE interaction by isothermal titration calorimetry (Figure 7 and Table 3). Injection of EntE into a solution containing 10 μM EntA resulted in a binding isotherm describing binding at two independent sites, each with a stoichiometry of ~1, indicating 1:1 EntA−EntE subunit interactions. Our sedimentation velocity analytical ultracentrifugation experiments showed that the distributions of the EntA dimer and tetramer at 10 °C were similar to those observed at 20 °C, and therefore at 10 μM EntA (the concentration used in our ITC experiment), there is a significant proportion [> 40% (see the inset of Figure 6A)] of the protein in the tetrameric form. Thus, the simplest explanation for the two binding sites that we observed by ITC is that the high-affinity binding site (Table 3, site 2) represents binding of EntE to tetrameric EntA, whereas the low-affinity binding site (Table 3, site 1) represents binding of EntE to dimeric EntA. Care must be taken in directly comparing for the EntA−EntE complex the absolute values of the equilibrium binding constants obtained by ITC with the $K_{0.5}$ value obtained by our fluorescence-based equilibrium binding assay because the ITC experiment had to be performed at 10 °C while the fluorescence-based assays were performed at the more physiologically relevant temperature of 20 °C. Given that, our ITC experiment clearly detected the presence of a low-affinity binding site and a high-affinity binding site in an EntA solution containing a mixture of EntA dimers and EntA tetramers, which is consistent with the effect of EntA concentration on the EntA−EntE binding signal that we measured by fluorescence, and also consistent with the EntA dimer−tetramer equilibrium detected by our AUC experiments.

When taken together, our experimental data demonstrate that EntE interacts with EntA and appears to form a higher-affinity complex with EntA in the tetrameric form compared to EntA in the dimeric form. Our cross-linking experiment detected only a

Scheme 3: Proposed Mechanism of Assembly of the EntA−EntE and EntE−holo-EntB Complexes during Enterobactin Biosynthesis[a]

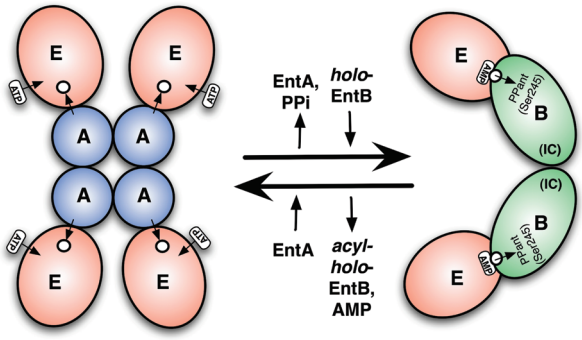

[a]In the first half-reaction, four EntE monomers (red ellipsoids) bind with optimal affinity to one EntA tetramer (blue circles indicate EntA monomers). Channeling then occurs in which DHB (small circles) produced by EntA is directly transferred to the EntE active site. Subsequent to DHB binding, ATP will bind at the EntE active site. While in complex with EntA, EntE catalyzes the production of the DHB−AMP species, followed by release of pyrophosphate (PP_i) and EntA. In the second half-reaction, holo-EntB [subunits shown as green elliposids; dimerization occurring through isochorismatase (IC) domains, consistent with the EntB crystal structure (PDB entry 2FQ1)] as an NRPS substrate forms a complex with the EntE−DHB−AMP species. DHB is then directly transferred to the phosphopantetheine (PPant) group attached to Ser245 of EntB, resulting in the production of acyl-holo-EntB. EntE and AMP dissociate from acyl-holo-EntB, allowing it to participate in downstream NRPS steps. Dissociated EntE could then again form a complex with an EntA tetramer, followed by another round of DHB adenylation upon binding of DHB (via transfer from EntA) and ATP.

large (> 250 kDa) cross-linked species that contained both EntA and EntE (Figure S1 of the Supporting Information). This would correspond to a complex comprised of four EntE monomers binding to one EntA tetramer (~360 kDa), which agrees with the stoichiometry of formation of the EntA−EntE complex revealed by our ITC experiments (i.e., 1:1 subunit−subunit binding). The effect of intracellular concentration on the oligomeric state of EntA may thus play a regulatory role during enterobactin biosynthesis, with activation of the process occurring upon EntA tetramerization only at sufficiently high intracellular concentrations following its expression after Fur derepression. Our pull-down assays also showed that recombinant EntE bait could pull down both chromosomally expressed EntA and EntB in situ from *E. coli* lysates when exogenous DHB was present. This supports our previous study (*32*) in which we showed that the EntE−EntB interaction affinity increases significantly in the presence of exogenous DHB, because of DHB binding to EntB as an allosteric regulator. The most likely explanation for our pull-down data is that EntA and EntB formed discrete and independent complexes with the immobilized EntE bait during the pull-down experiment. Consistent with this, we observed that EntA bait could pull down EntE but not EntB and, in our previous study, that EntB bait could pull down EntE but not EntA. To summarize our findings in the context of what is currently known about EntA, EntE, and EntB, we propose in Scheme 3 a model outlining the roles of dynamic protein−protein interactions in enterobactin biosynthetic steps involving EntE. In this model, EntE initially forms an optimal affinity complex with tetrameric EntA, facilitating direct channeling of DHB from EntA to the EntE active site. ATP would then enter the EntE active site, and the first half-reaction

(adenylation of DHB) would occur at an optimal rate along with release of pyrophosphate. EntA would then dissociate from EntE (subsequent to ATP hydrolysis), thus allowing the EntE−DHB−AMP complex to interact with the NRPS substrate holo-EntB. Direct transfer of the DHB moiety to PPant-Ser245 would then occur, resulting in the formation of acyl-holo-EntB followed by release of AMP. Dissociation of acyl-holo-EntB from EntE would then allow the DHB moiety to be transferred to the NRPS substrate holo-EntF for condensation with activated L-serine. Upon dissociation of acyl-holo-EntB, the EntE−EntA complex would be regenerated, resulting in turnover of the process. This model is consistent with recent reports elucidating the EntE mechanism in the context of its two half-reactions (*39*, *40*), such that the EntA−EntE interaction enhances the first half-reaction (formation of the DHB−AMP species at the active site of EntE), followed by the obligate EntE−holo-EntB interaction necessary for the transfer of DHB to holo-EntB Ser245. Our findings are also relevant in terms of what is now known about the superfamily to which EntE belongs, which has recently been designated the ANL superfamily (encompassing acyl-CoA synthetases, NRPS adenylation domains, and luciferases) (*58*). It has been shown that adenylation domains within this superfamily undergo significant conformational changes during catalysis, in a process termed domain alternation, to switch catalytic modes between an adenylate-forming conformation and a conformation that will facilitate subsequent thioester formation. For example, the C-terminal domain 4-chlorobenzoate:CoA ligase has been shown to undergo a 140° rotation subsequent to adenylate formation, rendering the enzyme competent for thioester formation with a CoA molecule bound to the same protein (*59*). In the case of EntE, acceleration of the rate of adenylate formation in the presence of EntA may be due to its stabilization of EntE in the adenylate-forming conformation, thus preventing domain alternation [i.e., repositioning of the A8 loop into the EntE active site (*31*)] until ATP hydrolysis has occurred. Dissociation of EntA would then facilitate EntE domain alternation, thus allowing for formation of the NRPS-obligate complex with the holo-EntB substrate. It is worth investigating whether protein−protein interactions modulate domain alternation in other free-standing adenylation domains such as DhbE, involved in bacillibactin biosynthesis in *Bacillus subtilis* (*37*), and BasE, which is involved in acinetobactin biosynthesis in *Acinetobacter baumannii* (*60*).

Here we have shown that *E. coli* enterobactin biosynthesis involves protein−protein interactions beyond the previously reported obligate interactions required for NRPS. We have established that there is a direct link between the terminal enzyme activity involved in DHB synthesis (EntA) and the NRPS enzyme EntE. Our study, in conjunction with previous reports, provides strong evidence that EntE has evolved such that its enzymatic activity is only fully optimized when the protein is participating in a protein−protein interaction that facilitates conformational remodeling of the EntE active site. We are now performing experiments to investigate the formation and coordination of the EntA−EntE and EntE−EntB complexes in vivo, and their effects on the efficiency of enterobactin biosynthesis (i.e., does formation of the EntA−EntE complex result in the channeling of DHB, or does formation of this complex serve to coordinate domain alternation in concert with holo-EntB, or both?). It has recently been reported that an endogenous catecholate siderophore is produced in mammals, with a homologue of *E. coli* EntA (BDH2) being essential for its biosynthesis; furthermore, a mammalian homologue of *E. coli* EntE has also been identified (*61*). Elucidation of the protein−protein interaction network necessary for *E. coli* enterobactin biosynthesis therefore provides not only further insights into a biological process that is essential for bacterial survival under iron-limiting conditions but also insights useful in interpreting the newly identified BDH2-dependent system that has been shown to play a role in mammalian iron homeostasis.

ACKNOWLEDGMENT

We thank Drs. Jack and Judith Kornblatt for their helpful discussions regarding the experiments presented in this study. We also thank Michael Lowden and Vasken Parsekhian for a critical reading of the manuscript. The Concordia Centre for Structural and Functional Genomics is also acknowledged for providing access to their Beckman XL-I analytical ultracentrifuge and to their Microcal VP-ITC microcalorimeter. P.D.P. also acknowledges the Quebec research networks GRASP and PROTEO, of which he is a member, for facilitating helpful discussions with colleagues through meetings and symposia.

SUPPORTING INFORMATION AVAILABLE

Peptides identified by LC−MS/MS after recovery from protein bands obtained from pull-down assays (Table S1), peptides identified by LC−MS/MS after recovery from a protein band obtained from an SMCC cross-linking experiment (Table S2), sedimentation velocity AUC data for EntA at 10 °C (Table S3), SDS−polyacrylamide gel of EntA and EntE covalently cross-linked by SMCC (Figure S1), and SDS−polyacrylamide gel of a control cross-linking reaction involving EntE and BSA (with and without maleimide activation by SMCC) (Figure S2). This material is available free of charge via the Internet at http://pubs.acs.org.

REFERENCES

1. Miethke, M., and Marahiel, M. A. (2007) Siderophore-based iron acquisition and pathogen control. *Microbiol. Mol. Biol. Rev. 71*, 413–451.
2. Crumbliss, A. L., and Harrington, J. M. (2009) Iron sequestration by small molecules: Thermodynamic and kinetic studies of natural siderophores and synthetic model compounds. *Adv. Inorg. Chem. 61*, 179–250.
3. Dam, T. (2005) Siderophores: Potential candidate in the therapy of neonatal meningitis. *J. Med. Microbiol. 54*, 613.
4. Wiles, T. J., Kulesus, R. R., and Mulvey, M. A. (2008) Origins and virulence mechanisms of uropathogenic *Escherichia coli*. *Exp. Mol. Pathol. 85*, 11–19.
5. Flo, T. H., Smith, K. D., Sato, S., Rodriguez, D. J., Holmes, M. A., Strong, R. K., Akira, S., and Aderem, A. (2004) Lipocalin 2 mediates an innate immune response to bacterial infection by sequestrating iron. *Nature 432*, 917–921.
6. Fischbach, M. A., Lin, H., Liu, D. R., and Walsh, C. T. (2006) How pathogenic bacteria evade mammalian sabotage in the battle for iron. *Nat. Chem. Biol. 2*, 132–138.
7. Fischbach, M. A., Lin, H., Zhou, L., Yu, Y., Abergel, R. J., Liu, D. R., Raymond, K. N., Wanner, B. L., Strong, R. K., Walsh, C. T., Aderem, A., and Smith, K. D. (2006) The pathogen-associated *iroA* gene cluster mediates bacterial evasion of lipocalin 2. *Proc. Natl. Acad. Sci. U.S.A. 103*, 16502–16507.
8. O'Brien, I. G., and Gibson, F. (1970) The structure of enterochelin and related 2,3-dihydroxy-N-benzoylserine conjugates from *Escherichia coli*. *Biochim. Biophys. Acta 215*, 393–402.
9. Raymond, K. N., Dertz, E. A., and Kim, S. S. (2003) Enterobactin: An archetype for microbial iron transport. *Proc. Natl. Acad. Sci. U.S.A. 100*, 3584–3588.
10. Harris, W. R., Carrano, C. J., Cooper, S. R., Sofen, S. R., Avdeef, A. E., McArdle, J. V., and Raymond, K. N. (1979) Coordination chemistry of microbial iron transport compounds. 19. Stability

constants and electrochemical behavior of ferric enterobactin and model complexes. *J. Am. Chem. Soc. 101*, 6097–6104.
11. Braun, V., and Killmann, H. (1999) Bacterial solutions to the iron-supply problem. *Trends Biochem. Sci. 24*, 104–109.
12. Stojiljkovic, I., and Hantke, K. (1995) Functional domains of the *Escherichia coli* ferric uptake regulator protein (Fur). *Mol. Gen. Genet. 247*, 199–205.
13. Sheikh, M. A., and Taylor, G. L. (2009) Crystal structure of the *Vibrio cholerae* ferric uptake regulator (Fur) reveals insights into metal co-ordination. *Mol. Microbiol. 72*, 1208–1220.
14. Carpenter, B. M., Whitmire, J. M., and Merrell, D. S. (2009) This is not your mother's repressor: The complex role of fur in pathogenesis. *Infect. Immun. 77*, 2590–2601.
15. Ozenberger, B. A., Brickman, T. J., and McIntosh, M. A. (1989) Nucleotide sequence of *Escherichia coli* isochorismate synthetase gene *entC* and evolutionary relationship of isochorismate synthetase and other chorismate-utilizing enzymes. *J. Bacteriol. 171*, 775–783.
16. Rusnak, F., Liu, J., Quinn, N., Berchtold, G. A., and Walsh, C. T. (1990) Subcloning of the enterobactin biosynthetic gene *entB*: Expression, purification, characterization, and substrate specificity of isochorismatase. *Biochemistry 29*, 1425–1435.
17. Liu, J., Duncan, K., and Walsh, C. T. (1989) Nucleotide sequence of a cluster of *Escherichia coli* enterobactin biosynthesis genes: Identification of *entA* and purification of its product 2,3-dihydro-2,3-dihydroxybenzoate dehydrogenase. *J. Bacteriol. 171*, 791–798.
18. Coderre, P. E., and Earhart, C. F. (1989) The *entD* gene of the *Escherichia coli* K12 enterobactin gene cluster. *J. Gen. Microbiol. 135*, 3043–3055.
19. Staab, J. F., Elkins, M. F., and Earhart, C. F. (1989) Nucleotide sequence of the *Escherichia coli entE* gene. *FEMS Microbiol. Lett. 50*, 15–19.
20. Rusnak, F., Sakaitani, M., Drueckhammer, D., Reichert, J., and Walsh, C. T. (1991) Biosynthesis of the *Escherichia coli* siderophore enterobactin: Sequence of the *entF* gene, expression and purification of EntF, and analysis of covalent phosphopantetheine. *Biochemistry 30*, 2916–2927.
21. Crosa, J. H., and Walsh, C. T. (2002) Genetics and assembly line enzymology of siderophore biosynthesis in bacteria. *Microbiol. Mol. Biol. Rev. 66*, 223.
22. Lai, J. R., Fischbach, M. A., Liu, D. R., and Walsh, C. T. (2006) A protein interaction surface in nonribosomal peptide synthesis mapped by combinatorial mutagenesis and selection. *Proc. Natl. Acad. Sci. U. S.A. 103*, 5314–5319.
23. Chen, D., Wu, R., Bryan, T. L., and Dunaway-Mariano, D. (2009) *In vitro* kinetic analysis of substrate specificity in enterobactin biosynthetic lower pathway enzymes provides insight into the biochemical function of the hot dog-fold thioesterase EntH. *Biochemistry 48*, 511–513.
24. Guo, Z. F., Sun, Y., Zheng, S., and Guo, Z. (2009) Preferential hydrolysis of aberrant intermediates by the type II thioesterase in *Escherichia coli* nonribosomal enterobactin synthesis: Substrate specificities and mutagenic studies on the active-site residues. *Biochemistry 48*, 1712–1722.
25. Furrer, J. L., Sanders, D. N., Hook-Barnard, I. G., and McIntosh, M. A. (2002) Export of the siderophore enterobactin in *Escherichia coli*: Involvement of a 43 kDa membrane exporter. *Mol. Microbiol. 44*, 1225–1234.
26. Gavin, A. C., Bösche, M., Krause, R., Grandi, P., Marzioch, M., Bauer, A., Schultz, J., Rick, J. M., Michon, A. M., Cruciat, C. M., Remor, M., Höfert, C., Schelder, M., Brajenovic, M., Ruffner, H., Merino, A., Klein, K., Hudak, M., Dickson, D., Rudi, T., Gnau, V., Bauch, A., Bastuck, S., Huhse, B., Leutwein, C., Heurtier, M. A., Copley, R. R., Edelmann, A., Querfurth, E., Rybin, V., Drewes, G., Raida, M., Bouwmeester, T., Bork, P., Seraphin, B., Kuster, B., Neubauer, G., and Superti-Furga, G. (2002) Functional organization of the yeast proteome by systematic analysis of protein complexes. *Nature 415*, 141–147.
27. Devos, D., and Russell, R. B. (2007) A more complete, complexed and structured interactome. *Curr. Opin. Struct. Biol. 17*, 370–377.
28. Bagnasco, L., Tortolina, L., Biasotti, B., Castagnino, N., Ponassi, R., Tomati, V., Nieddu, E., Stier, G., Malacarne, D., and Parodi, S. (2007) Inhibition of a protein-protein interaction between INI1 and c-Myc by small peptidomimetic molecules inspired by Helix-1 of c-Myc: Identification of a new target of potential antineoplastic interest. *FASEB J. 21*, 1256–1263.
29. Wells, J. A., and McClendon, C. L. (2007) Reaching for high-hanging fruit in drug discovery at protein-protein interfaces. *Nature 450*, 1001–1009.
30. Lai, J. R., Fischbach, M. A., Liu, D. R., and Walsh, C. T. (2006) Localized protein interaction surfaces on the EntB carrier protein revealed by combinatorial mutagenesis and selection. *J. Am. Chem. Soc. 128*, 11002–11003.
31. Drake, E. J., Nicolai, D. A., and Gulick, A. M. (2006) Structure of the EntB multidomain nonribosomal peptide synthetase and functional analysis of its interaction with the EntE adenylation domain. *Chem. Biol. 13*, 409–419.
32. Khalil, S., and Pawelek, P. D. (2009) Ligand-induced conformational rearrangements promote interaction between the *Escherichia coli* enterobactin biosynthetic proteins EntE and EntB. *J. Mol. Biol. 393*, 658–671.
33. Ehmann, D. E., Shaw-Reid, C. A., Losey, H. C., and Walsh, C. T. (2000) The EntF and EntE adenylation domains of *Escherichia coli* enterobactin synthetase: Sequestration and selectivity in acyl-AMP transfers to thiolation domain cosubstrates. *Proc. Natl. Acad. Sci. U. S.A. 97*, 2509–2514.
34. Sundlov, J. A., Garringer, J. A., Carney, J. M., Reger, A. S., Drake, E. J., Duax, W. L., and Gulick, A. M. (2006) Determination of the crystal structure of EntA, a 2,3-dihydro-2,3-dihydroxybenzoic acid dehydrogenase from *Escherichia coli*. *Acta Crystallogr. D62*, 734–740.
35. Rusnak, F., Faraci, W. S., and Walsh, C. T. (1989) Subcloning, expression, and purification of the enterobactin biosynthetic enzyme 2,3-dihydroxybenzoate-AMP ligase: Demonstration of enzyme-bound (2,3-dihydroxybenzoyl)adenylate product. *Biochemistry 28*, 6827–6835.
36. Gehring, A. M., Mori, I., and Walsh, C. T. (1998) Reconstitution and characterization of the *Escherichia coli* enterobactin synthetase from EntB, EntE, and EntF. *Biochemistry 37*, 2648–2659.
37. May, J. J., Kessler, N., Marahiel, M. A., and Stubbs, M. T. (2002) Crystal structure of DhbE, an archetype for aryl acid activating domains of modular nonribosomal peptide synthetases. *Proc. Natl. Acad. Sci. U.S.A. 99*, 12120–12125.
38. Neres, J., Wilson, D. J., Celia, L., Beck, B. J., and Aldrich, C. C. (2008) Aryl acid adenylating enzymes involved in siderophore biosynthesis: Fluorescence polarization assay, ligand specificity, and discovery of non-nucleoside inhibitors via high-throughput screening. *Biochemistry 47*, 11735–11749.
39. Sikora, A. L., Wilson, D. J., Aldrich, C. C., and Blanchard, J. S. (2010) Kinetic and inhibition studies of dihydroxybenzoate-AMP ligase from *Escherichia coli*. *Biochemistry 49*, 3648–3657.
40. Sikora, A. L., Cahill, S. M., and Blanchard, J. S. (2009) Enterobactin synthetase-catalyzed formation of P^1,P^3-diadenosine-5′-tetraphosphate. *Biochemistry 48*, 10827–10829.
41. Kitagawa, M., Ara, T., Arifuzzaman, M., Ioka-Nakamichi, T., Inamoto, E., Toyonaga, H., and Mori, H. (2005) Complete set of ORF clones of *Escherichia coli* ASKA library (a complete set of *E. coli* K-12 ORF archive): Unique resources for biological research. *DNA Res. 12*, 291–299.
42. Philo, J. S. (2006) Improved methods for fitting sedimentation coefficient distributions derived by time-derivative techniques. *Anal. Biochem. 354*, 238–246.
43. Shuck, P. (2003) On the analysis of protein self-association by sedimentation velocity analytical ultracentrifugation. *Anal. Biochem. 320*, 104–124.
44. García De La Torre, J., Huertas, M. L., and Carrasco, B. (2000) Calculation of hydrodynamic properties of globular proteins from their atomic-level structure. *Biophys. J. 78*, 719–730.
45. Hayes, D. B., Laue, T., and Philo, J. S. (1995) Sednterp: Sedimentation Interpretation Program, Alliance Protein Laboratories, Thousand Oaks, CA.
46. Sousa, E. H., Garay, P. A., Tinianow, J. N., and Gerber, N. C. (2006) Development of a spectrophotometric assay for cyclase activity. *Anal. Biochem. 348*, 57–63.
47. Lakowicz, J. R. (2006) Principles of Fluorescence Spectroscopy, 3rd ed., Springer, Berlin.
48. Stafford, W. F. (2000) Analysis of reversibly interacting macromolecular systems by time derivative sedimentation velocity. *Methods Enzymol. 323*, 302–325.
49. Geipel, G., Acker, M., Vulpius, D., Bernhard, G., Nitsche, H., and Fanghänel, T. (2004) An ultrafast time-resolved fluorescence spectroscopy system for metal ion complexation studies with organic ligands. *Spectrochim. Acta, Part A 60*, 417–424.
50. Cole, J. L. (1996) Characterization of human cytomegalovirus protease dimerization by analytical centrifugation. *Biochemistry 35*, 15601–15610.
51. Srere, P. A. (1987) Complexes of sequential metabolic enzymes. *Annu. Rev. Biochem. 56*, 89–124.
52. Jørgensen, K., Rasmussen, A. V., Morant, M., Nielsen, A. H., Bjarnholt, N., Zagrobelny, M., Bak, S., and Møller, B. L. (2005) Metabolon formation and metabolic channeling in the biosynthesis of plant natural products. *Curr. Opin. Plant Biol. 8*, 280–291.

53. Durek, P., and Walther, D. (2008) The integrated analysis of metabolic and protein interaction networks reveals novel molecular organizing principles. *BMC Syst. Biol. 2*, 100.
54. An, S., Kumar, R., Sheets, E. D., and Benkovic, S. J. (2008) Reversible compartmentalization of *de novo* purine biosynthetic complexes in living cells. *Science 320*, 103–106.
55. Fukushima, T., Decker, R. V., Anderson, W. M., and Spivey, H. O. (1989) Substrate channeling of NADH and binding of dehydrogenases to complex I. *J. Biol. Chem. 264*, 16483–16488.
56. Spivey, H. O., and Ovádi, J. (1999) Substrate channeling. *Methods 19*, 306–321.
57. Lambalot, R. H., Gehring, A. M., Flugel, R. S., Zuber, P., LaCelle, M., Marahiel, M. A., Reid, R., Khosla, C., and Walsh, C. T. (1996) A new enzyme superfamily: The phosphopantetheinyl transferases. *Chem. Biol. 3*, 923–936.
58. Gulick, A. M. (2009) Conformational dynamics in the acyl-CoA synthetases, adenylation domains of non-ribosomal peptide synthetases, and firefly luciferase. *ACS Chem. Biol. 4*, 811–827.
59. Reger, A. S., Wu, R., Dunaway-Mariano, D., and Gulick, A. M. (2008) Structural characterization of a 140° domain movement in the two-step reaction catalyzed by 4-chlorobenzoate:CoA ligase. *Biochemistry 47*, 8016–8025.
60. Drake, E. J., Duckworth, B. P., Neres, J., Aldrich, C. C., and Gulick, A. M. (2010) Biochemical and structural characterization of bisubstrate inhibitors of BasE, the self-standing nonribosomal peptide synthetase adenylate-forming enzyme of acinetobactin synthesis. *Biochemistry 49*, 9292–9305.
61. Devireddy, L. R., Hart, D. O., Goetz, D. H., and Green, M. R. (2010) A mammalian siderophore synthesized by an enzyme with a bacterial homolog involved in enterobactin production. *Cell 141*, 1006–1017.